Journal of Computational Physics 316 (2016) 180–192

Contents lists available at ScienceDirect

Journal of Computational Physics

www.elsevier.com/locate/jcp

A gyrokinetic continuum code based on the numerical Lie transform (NLT) method

Lei Ye [a], Yingfeng Xu [a], Xiaotao Xiao [a], Zongliang Dai [b], Shaojie Wang [b,*]

[a] Institute of Plasma Physics, Chinese Academy of Science, Hefei, Anhui 230031, China
[b] Department of Modern Physics, University of Science and Technology of China, Hefei, Anhui 230026, China

ARTICLE INFO

Article history:
Received 2 October 2015
Received in revised form 26 February 2016
Accepted 3 March 2016
Available online 14 April 2016

Keywords:
Gyrokinetic simulation
Numerical Lie transform
Semi-Lagrangian
High dimensional interpolation

ABSTRACT

In this work, we report a novel gyrokinetic simulation method named numerical Lie transform (NLT), which depends on a new physical model derived from the I-transform theory. In this model, the perturbed motion of a particle is decoupled from the unperturbed motion. Due to this property, the unperturbed orbit can be computed in advance and saved as numerical tables for real-time computation. A 4D tensor B-spline interpolation module is developed and applied with the semi-Lagrangian scheme to avoid operator splitting. The NLT code is verified by the Rosenbluth–Hinton test and the linear ITG Cyclone test.

1. Introduction

Plasma transport is one of the most critical scientific challenges for controlled fusion [1]. In magnetically confined plasmas, it is generally accepted that drift wave turbulence, which originates from the free energy provided by the spatial gradients of plasma temperature and density, determines the transport properties of particles and thermal energy [2]. In most cases this type of turbulence appears as the saturation state of small amplitude fluctuations, which are driven by the small scale ($k\rho \sim 1$) and low frequency ($\omega \ll \omega_c$) micro-instabilities. Here, k is wave number, ω is wave frequency, ρ and ω_c are particle gyro-radius and gyro-frequency, respectively. The drift wave turbulence is complex and essentially nonlinear so that particular difficulties arise for analytical theories. Therefore, numerical simulation has become a powerful tool in addition to experimental investigation to study the turbulent transport in plasma physics.

During the past decades, significant progress has been made in plasma turbulence simulation [3] and the most successful physical model is based on the gyrokinetic theory. The basic idea of gyrokinetic theory [4] is to decouple the fast gyro-motion of a particle from the slow drift motion of the gyro-center. For numerical simulation, one of the main benefits of this theory is that six-dimensional particle phase space is reduced to four-dimensional gyro-center phase space (though the gyro-center distribution function is five-dimensional), which significantly saves the computational effort. Another one is that the time step size for the computation can be greatly enlarged ($\omega_c \Delta t > 1$) due to the averaging-out of the fast gyro-motion. The gyrokinetic model is composed of the gyrokinetic equation (GKE), which describes the evolution of gyro-center distribution, and the gyrokinetic field equations which determine the self-consistent electromagnetic fields. Up to now, the numerical methods that have been used to solve the GKE can be classified into three types [5]: the Lagrangian approach (also referred to as PIC) [6–8], the Eulerian approach [9–11] and the semi-Lagrangian approach

* Corresponding author.
E-mail address: wangsj@ustc.edu.cn (S. Wang).

http://dx.doi.org/10.1016/j.jcp.2016.03.068
0021-9991/

[12–14] which will be focused primarily in this paper. In the semi-Lagrangian method the distribution function, which is discretized on a fixed phase space grid, can be updated by integrating the perturbed orbit backward at each time step and then interpolating the value of the distribution function at the origin of the orbit. For the gyro-center dynamics, a high dimensional (4D) interpolation technique is needed if one follows the full gyro-center orbit. Hence there are usually two main components in a semi-Lagrangian GKE solver, the perturbed orbit integration and the phase space interpolation. For most of the semi-Lagrangian codes [12–14], on one hand, the orbit calculation must be performed in each time step with the time-dependent perturbed fields. On the other hand, due to the complexity of high dimensional interpolation, the operator splitting method [15], which transforms a high dimensional equation to a set of low dimensional equations, is incorporated with the semi-Lagrangian scheme to avoid 4D phase space interpolation. This operator splitting method, though make numerical implementation much easier, may introduce additional numerical error [16] which can bring about spurious dissipation. Moreover, an improper splitting scheme may break the Hamiltonian property of gyro-center dynamics, such as the conservation of phase-space volume.

Recently, a new method to solve the gyrokinetic equation is developed by introducing the I-transform [17–19], which is essentially a special Lie transform. The key idea of the I-transform is to decouple the perturbed motion of the gyro-center from the unperturbed motion. With this new theory, a single particle orbit code with the electromagnetic perturbation [20] and a continuum code which solves the 1D Vlasov–Possion system have been developed [21]. These two codes have been verified by GYCAVA code [22] and the conservative semi-Lagrangian code, respectively. In this paper, we extend our work to carry out the electrostatic turbulence simulation in tokamak geometry. There are two distinct differences between our code and previous semi-Lagrangian codes. Firstly, only unperturbed orbit is needed in our simulation since the perturbed motion has been decoupled by the I-transform. Thus the unperturbed orbit, which is determined by time-independent equilibrium field, can be computed only once and saved as numerical tables for real-time computation. Secondly, we use 4D interpolation by tensor product B-splines to avoid operator splitting.

The remaining part of this paper is organized as follows. In Section 2, the fundamental equations are introduced. In Section 3, the numerical methods for solving both the GKE and the quasi-neutrality equation are described. In Section 4, the numerical simulation results are presented and discussed. Finally, we summarize the main results in Section 5.

2. Fundamental equations

In a collisionless plasma, the particle distribution function $F(\boldsymbol{Z}, t)$ in gyro-center coordinates $Z = (\boldsymbol{X}, v_\parallel, \mu)$ satisfies the gyrokinetic Vlasov equation, which is written as

$$\frac{d}{dt}F = \frac{\partial F}{\partial t} + \dot{\boldsymbol{X}}\frac{\partial F}{\partial \boldsymbol{X}} + \dot{v}_\parallel \frac{\partial F}{\partial v_\parallel} = 0, \tag{1}$$

with $\boldsymbol{X}$ the position of gyro-center, $v_\parallel$ the parallel velocity of the particle and μ the magnetic moment. Here, the total time derivative $\frac{d}{dt}$ in Eq. (1) is taken along the gyro-center orbit in phase space, which indicates that following the gyro-center trajectory the distribution function is a constant. Clearly, Eq. (1) is a convective equation and its characteristic is just the gyro-center orbit in an electromagnetic field, which includes both equilibrium and perturbation fields.

In this section, a brief introduction to the I-transform method and the GKE are given. For more details on the I-transform method, we refer the reader to Refs. [17–19].

2.1. Magnetic equilibrium configuration and unperturbed equations of motion

The equilibrium magnetic field in a tokamak can be written in either a contravariant or a covariant form as [23]

$$\begin{aligned}\boldsymbol{B_0} &= q(\psi)\nabla\psi \times \nabla\theta + \nabla\zeta \times \nabla\psi \\ &= g(\psi)\nabla\zeta + I(\psi)\nabla\theta + g(\psi)\delta(\psi,\theta)\nabla\psi,\end{aligned} \tag{2}$$

where (ψ, θ, ζ) are the magnetic flux coordinates, with ψ the poloidal magnetic flux, θ the poloidal angle, and ζ the toroidal angle. $q(\psi)$ is the safety factor. $2\pi\mu_0 g(\psi)$ is the poloidal current outside ψ; $2\pi\mu_0 I(\psi)$ is the total current inside ψ. $\delta(\psi,\theta)$ is related to the non-orthogonality of $\nabla\psi$ and $\nabla\theta$. The metric coefficients of the magnetic flux coordinates (ψ, θ, ζ) can be defined by

$$g^{\psi\psi} = |\nabla\psi|^2, g^{\psi\theta} = g^{\theta\psi} = \nabla\psi\cdot\nabla\theta, g^{\theta\theta} = |\nabla\theta|^2.$$

The Jacobian of the configuration coordinate is

$$\mathcal{J} = |\nabla\psi \times \nabla\theta \cdot \nabla\zeta|^{-1} = \frac{qg + I}{B^2}. \tag{3}$$

The unperturbed Poisson bracket, which determines unperturbed guiding-center (GC) motion, is expressed in the GC phase space coordinates $(\boldsymbol{X}, v_\parallel, \mu, \xi)$ as

$$\{K,G\}=\frac{e_s}{m_s}\left(\frac{\partial K}{\partial \xi}\frac{\partial G}{\partial \mu}-\frac{\partial K}{\partial \mu}\frac{\partial G}{\partial \xi}\right)+\frac{\mathbf{B}_0^*}{m_s B_{0\|}^*}\cdot\left(\nabla K\frac{\partial G}{\partial v_\|}-\frac{\partial K}{\partial v_\|}\nabla G\right)-\frac{\mathbf{b}_0}{e_s B_{0\|}^*}\cdot\nabla K\times\nabla G \tag{4}$$

with ξ the gyro-angle, $\mathbf{B}_0^*=\mathbf{B}_0+\frac{m_s v_\|}{e_s}\nabla\times\mathbf{b}_0$ and $B_{0\|}^*=\mathbf{b}_0\cdot\mathbf{B}_0^*$. The subscript s denotes the species of the particle. The Jacobian of the GC phase space coordinates $(\boldsymbol{X}, v_\|, \mu, \xi)$ is expressed as

$$\mathcal{J}^*=\frac{B_{0\|}^*}{m_s}. \tag{5}$$

For equilibrium magnetic field given by Eq. (2), the non-zero components of the Poisson matrix in the GC phase space coordinates $\boldsymbol{Z}_0=(\psi,\theta,\zeta,v_\|,\mu,\xi)$ can be written as

$$J^{\psi v_\|}=-J^{v_\|\psi}=\frac{v_\|B}{e_sD}\partial_\theta\frac{g}{B}, \tag{6}$$

$$J^{\theta v_\|}=-J^{v_\|\theta}=\frac{B}{m_sD}\left(1-\frac{m_sv_\|}{e_s}\partial_\psi\frac{g}{B}\right), \tag{7}$$

$$J^{\zeta v_\|}=-J^{v_\|\zeta}=\frac{B}{m_sD}\left[q+\frac{m_sv_\|}{e_s}\left(\partial_\psi\frac{I}{B}-\partial_\theta\frac{g\delta}{B}\right)\right], \tag{8}$$

$$J^{\psi\theta}=-J^{\theta\psi}=-\frac{g}{e_sD}, \tag{9}$$

$$J^{\psi\zeta}=-J^{\zeta\psi}=\frac{I}{e_sD}, \tag{10}$$

$$J^{\theta\zeta}=-J^{\zeta\theta}=-\frac{g\delta}{e_sD}, \tag{11}$$

$$J^{\xi\mu}=-J^{\mu\xi}=\frac{e_s}{m_s}, \tag{12}$$

with $D=qg+I+\rho_\|(I'g-g'I)-\rho_\|g^2\partial_\theta\delta$ and $\rho_\|=m_sv_\|/e_sB$. The phase space Jacobian of $\boldsymbol{Z}_0$ is $\mathcal{J}^*=D/m_sB$.

The unperturbed equations of motion can be given by

$$\dot{Z}_0^i=J^{ij}\partial_jH_0, \tag{13}$$

with the unperturbed GC Hamiltonian

$$H_0=\frac{1}{2}m_sv_\|^2+\mu B_0+e_s\Phi_0.$$

2.2. The I-transform method

The I-transform we used here is a special Lie transform performed in a short time interval Δt. This transform assumes the following orderings

$$\epsilon_\delta\sim\frac{\delta F}{F_0}\ll 1,\ \epsilon_t\sim\omega\Delta t\sim k_\|v_\|\Delta t\ll 1,$$

with δF and F_0 the perturbed and the equilibrium distribution, respectively; $k_\|$ is the parallel wave number.

In a given time interval $[t_0, t_0+\Delta t]$, the I-transform perturbation method transforms the gyro-center coordinate $\boldsymbol{Z}$ to a new coordinates $\boldsymbol{z}$ so that the Poisson bracket as well as the equations of motion in $\boldsymbol{z}$ are formally identical to those in the unperturbed GC coordinates $\boldsymbol{Z}_0$, which are given by Eqs. (6)–(13). Consequently, in this time interval the GKE in the new coordinate $\boldsymbol{z}$ can be written as

$$\frac{d_0}{dt}f=0. \tag{14}$$

Here, f is the distribution function in $\boldsymbol{z}$ and the total time derivative $\frac{d_0}{dt}$ is taken along the unperturbed orbit which is determined by Eq. (13).

The relationship between coordinates $\boldsymbol{Z}$ and $\boldsymbol{z}$ can be expressed by the I-transform operator $\mathcal{T}$ as

$$z^i=\mathcal{T}Z^i. \tag{15}$$

While the gyro-center distribution function F can be transformed from f by the pull-back transform

$$F=\mathcal{T}^{-1}f. \tag{16}$$

Eqs. (14)–(16) are equivalent to the standard GKE, Eq. (1), for $t \in [t_0, t_0 + \Delta t]$. While for realistic calculation, the second order expansion of the I-transform operator is applied so that Eq. (15) and Eq. (16) can be written as

$$z^i = Z^i + G_1^i + \frac{1}{2} G_1^j \partial_j G_1^i + o(\epsilon_\delta^2 \epsilon_t^2) \tag{17}$$

$$F = f + \frac{1}{\mathcal{J}^*} \partial_i [\mathcal{J}^* (G_1^i + \frac{1}{2} G_1^i G_1^j \partial_j) F] + o(\epsilon_\delta^2 \epsilon_t^2). \tag{18}$$

Note that the G_2 terms are ignored in Eq. (17) and Eq. (18), which is correct for a short time I-transform [20].

Here, the 1st-order generating vector field $G_1(z,t)$ is an incompressible flow in the phase space which satisfies

$$\frac{1}{\mathcal{J}^*} \partial_i (\mathcal{J}^* G_1^i) = 0, \tag{19}$$

and can be calculated by

$$G_1^i = \partial_k S_1 J^{ki}. \tag{20}$$

$S_1(z,t)$ denotes the 1st-order gauge function of the I-transform, which in the electrostatic situation satisfies

$$\frac{d_0}{dt} S_1 = e_i \overline{\delta\phi}, \tag{21}$$

with $\delta\phi$ the perturbed electrostatic potential and $\overline{(\cdots)}$ the gyro-average operator defined by

$$\overline{\delta\phi}(\mathbf{X}, \mu, t) = \frac{1}{2\pi} \int_0^{2\pi} \delta\phi(\mathbf{X} + \boldsymbol{\rho}(\mu, \xi), t) d\xi. \tag{22}$$

For computational efficiency and numerical accuracy, the full distribution function f is decomposed into a perturbed part δf and an equilibrium part f_{eq}, which satisfies

$$\frac{d_0}{dt} f_{eq} = 0. \tag{23}$$

Therefore, with the help of Eq. (20) and Eq. (23), Eq. (14) and Eq. (18) reduce to

$$\frac{d_0}{dt} \delta f = 0, \tag{24}$$

$$\delta F = \delta f + G_1^i \partial_i f_{eq} + G_1^i \partial_i \delta f + \frac{1}{2} G_1^i \partial_i (G_1^j \partial_j)(\delta f + f_{eq}). \tag{25}$$

Note that the second term on the right hand side of Eq. (25) denotes the linear response, e.g. the usual $(\omega - \omega^*)$ term in the conventional gyrokinetic δf method, as has been clarified in Ref. [17]; the third term and the last term are the nonlinear effects, including the well-known $E \times B$ nonlinearity.

Since the I-transform is a short time transform in $t \in [t_0, t_0 + \Delta t]$, it must be performed for each time step in numerical simulation. And the initial condition for each time step are

$$\delta f(t_0) = \delta F(t_0) \tag{26}$$

$$S_1(t_0) = 0 \tag{27}$$

$$G_1(t_0) = 0 \tag{28}$$

Eqs. (20), (21), (24) and (25) are the GKEs of the I-transform theory in $[t_0, t_0 + \Delta t]$ with initial condition given by Eqs. (26), (27) and (28). Note that in comparison to Eq. (1), the total time derivatives in the I-transformed GKE are taken along the unperturbed orbit. This property can be used in numerical computation to reduce the computational effort, which is discussed in Sec. 3.

2.3. Gyrokinetic quasi-neutrality equation

The gyrokinetic quasi-neutrality (QN) equation is written as

$$\frac{e_i^2 \rho_i^2}{T_i} \nabla \cdot (n_{0i} \nabla_\perp \delta\phi) = -(e_i \delta n_i^g - e \delta n_e), \tag{29}$$

with $\rho_i = \sqrt{m_i T_i}/e_i B$ the gyro-radius, n_{0i} the equilibrium ion density, T_i the ion temperature. The left-hand side of Eq. (29) is the ion polarization density, with the long-wavelength approximation used. This approximation is valid for the ITG turbulence with adiabatic electrons [24].

The gyro-center density δn_i^g is expressed as

$$\delta n_i^g = \int \overline{\delta F} \frac{B_{0\|}^*}{m_i} d\xi d\mu dv_\| . \tag{30}$$

Here, the over-bar denotes the gyro-average operator defined by Eq. (22). The electrons are assumed adiabatic, so that the perturbed electron density can be expressed as

$$\delta n_e \simeq e n_{0e} \frac{\delta\phi - \langle\delta\phi\rangle}{T_e}, \tag{31}$$

where $\langle\cdots\rangle$ denotes the magnetic-flux-surface average. Inserting Eq. (31) into Eq. (29) and taking flux average on both sides we get the equation for $\langle\delta\phi\rangle$ as

$$\langle \frac{e_i^2 \rho_{ti}^2}{T_i} \nabla\cdot(n_{0i}\nabla_\perp \delta\phi)\rangle = -e_i \langle \delta n_i^g \rangle. \tag{32}$$

For flux coordinates (ψ,θ,ζ), the operator $\mathcal{L} \doteq \nabla\cdot(n_{0i}\nabla_\perp)$ in Eq. (29) can be expressed in large-aspect-ratio limit as

$$\mathcal{L} \simeq \frac{1}{J}[\partial_\psi(Jg^{\psi\psi} n_{0i}\partial_\psi) + \partial_\psi(Jg^{\psi\theta} n_{0i}\partial_\theta) + \partial_\theta(Jg^{\theta\psi} n_{0i}\partial_\psi) + \partial_\theta(Jg^{\theta\theta} n_{0i}\partial_\theta) - \partial_\theta(\frac{n_{0i}}{JB^2}\partial_\theta)]. \tag{33}$$

Note that in this limit, the operator $\mathcal{L}$ does not depend on the toroidal angle so that Eq. (29) actually becomes a 2D partial differential equation with ζ treated as a parameter. For a given toroidal angle ζ^*, the 2D QN equation with adiabatic electron response for $\delta\phi(\psi,\theta,\zeta^*)$ can be written as

$$(c_1\partial_{\psi^2}^2 + c_2\partial_{\theta^2}^2 + c_3\partial_{\psi\theta}^2 + c_4\partial_\psi + c_5\partial_\theta + c_6)\delta\phi(\psi,\theta,\zeta^*) = -(e_i\delta n_i^g(\psi,\theta,\zeta^*) + e n_{0e}\frac{e\langle\delta\phi\rangle}{T_e}. \tag{34}$$

The details of the coefficients $c_i(\psi,\theta)$ can be found in Appendix A. Similarly, Eq. (32) can be written as

$$(d_1\partial_{\psi^2}^2 + d_2\partial_\psi)\langle\delta\phi\langle(\psi,\zeta^*)\rangle = -e_i\langle\delta n_i^g\rangle, \tag{35}$$

where the coefficients $d_i(\psi)$ are also derived in Appendix A. Eq. (34) and Eq. (35) are the QN equations used in our simulation and the numerical scheme will be given in the next section.

3. Numerical implementation

A numerical tokamak equilibrium configuration [13,25] is used in the NLT code. The perturbed part of distribution function $\delta f(\psi,\theta,\zeta,V_\|,\mu)$ is discretized on an uniform phase space grid, which can be denoted as

$$\delta f(z_I) \doteq \delta f(\psi_i,\theta_j,\zeta_k,V_{\|l},\mu_m),$$

where i,j,k,l and m are grid indices for each coordinate. The discretizations of the gauge function S_1 and the generating vector field G_1 are the same as δf. The perturbed potential is discretized on the configuration grid, which is denoted by

$$\delta\phi_{i,j}^k = \delta\phi(\psi_i,\theta_j,\zeta_k).$$

3.1. GKEs solver

Eq. (21) and Eq. (24) are solved by using the backward semi-Lagrangian method. For a given time interval $[t^n, t^{n+1}]$, the value of the distribution function at a grid point is updated by tracing the phase space characteristic $z(t)$ from the grid $z(t^{n+1}) = z_I$ backward in time to find its point of origin, which is denoted by $z(t^n) = z_I^*$.

From Eq. (24), it is clear that

$$\delta f(z_I, t^{n+1}) = \delta f(z_I^*, t^n). \tag{36}$$

Thus $\delta f(z_I, t^{n+1})$ can be computed by a 4D tensor spline interpolation, which predicts the off-grid value $\delta f(z_I^*, t^n)$ from grid-point values $\delta f(z_I, t^n)$. The details about the 4D tensor spline interpolation can be found in Appendix B.

Compared with Eq. (24), there is an additional source term $\overline{\delta\phi(z,t)}$ on the right hand side of Eq. (21). Integrating Eq. (21) from t^n to t^{n+1}, one has

$$S_1(z_I,t^{n+1}) - S_1(z_I^*,t^n) = e_i \int_{t^n}^{t^{n+1}} \overline{\delta\phi(z(t),t)} dt.$$

Note that for each time step $[t^n, t^{n+1}]$ $S_1(z, t^n) = 0$ holds and $\delta F = \delta f$ at time $t = t^n$. The above integral can be evaluated by

$$\int_{t^n}^{t^{n+1}} \overline{\delta\phi(z(t), t)}dt = \overline{\delta\phi(z_I^*, t^n)}\Delta t + O(\Delta t^2).$$

So the numerical scheme for updating S_1 can be written as

$$S_1(z_I, t^{n+1}) = e_i\overline{\delta\phi(z_I^*, t^n)}\Delta t + O(\Delta t^2). \tag{37}$$

The numerical error analysis for this equation can be found in Ref. [20].

After updating δf and S_1 by Eq. (36) and Eq. (37), the gyro-center distribution δF can by explicitly calculated by Eq. (25). The partial derivatives therein are approximated by the fourth order central finite difference scheme, which can be written as

$$\frac{\partial f}{\partial x}\Big|_{x=x_i} = \frac{f_{i-2} - 8f_{i-1} + 8f_{i+1} - f_{i+2}}{12\Delta x} + O\left(\Delta x^4\right), \tag{38}$$

$$\frac{\partial f^2}{\partial^2 x}\Big|_{x=x_i} = \frac{-f_{i-2} + 16f_{i-1} - 30f_i + 16f_{i+1} - f_{i+2}}{12\Delta x^2} + O\left(\Delta x^4\right), \tag{39}$$

where x indicates ψ, θ, ζ and $v_\parallel$.

3.2. Midpoint predictor–corrector algorithm

The numerical integration scheme of Eq. (37) has only first-order accuracy in time. To improve the numerical accuracy, the midpoint predictor–corrector method is applied to the GKE solver. Let $t^{n+\frac{1}{2}} = (t^{n+1} + t^n)/2$. The characteristic $z(t)$ starting from $z(t^{n+1}) = z_I$ can be computed backward to $t = t^{n+\frac{1}{2}}$ and denoted by $z(t^{n+\frac{1}{2}}) = z_I'$. For a given time interval $[t^n, t^{n+1}]$, the predictor–corrector method for the GKE is applied as follows.

Predictor step:

Step 1. Compute $S_1(t^{n+\frac{1}{2}})$ and $\delta f(t^{n+\frac{1}{2}})$ from $\delta f(t^n)$, $S_1(t^n)$ and $\delta\phi(t^n)$ according to Eq. (36) and Eq. (37), where z_I^* is replaced by z_I'.

Step 2. Compute $\delta F(t^{n+\frac{1}{2}})$ by Eq. (25).

Step 3. Solve the QN equation to compute $\delta\phi(t^{n+\frac{1}{2}})$.

Corrector step:

Step 4. Compute $\delta f(t^{n+1})$ and $S_1(t^{n+1})$ from $\delta f(t^n)$, $S_1(t^n)$ and $\delta\phi(t^{n+\frac{1}{2}})$ according to Eq. (36) and Eq. (37). In this step, the perturbed potential in Eq. (37) should be replaced by the predicted value as

$$S_1(z_I, t^{n+1}) = e_i\overline{\delta\phi(z_I', t^{n+\frac{1}{2}})}\Delta t + O(\Delta t^3). \tag{40}$$

3.3. Quasi-neutrality equation solver

The 2D QN equation Eq. (34) is solved by using a combination of the pseudo-spectral method in poloidal direction and the finite difference method in radial direction. The partial differential equation is transformed to a linear equation set of $\delta\phi_{i,j}^k$, which is written as

$$Ax = b. \tag{41}$$

For the 1D flux-averaged QN Eq. (35), it can also be transformed into a linear algebraic equation set denoted by

$$\langle A\rangle\langle x\rangle = \langle b\rangle. \tag{42}$$

The details of the derivation of Eq. (41) and Eq. (42) can be found in Appendix C. The linear systems (41) and (42) are solved by the Gaussian elimination method. The inverse matrices of A and $\langle A\rangle$ are denoted by A^{-1} and $\langle A\rangle^{-1}$, respectively. These two matrices can be computed and saved in the initialization step. For real-time computation the QN equation can be solved by

$$\langle x\rangle = \langle A\rangle^{-1}\langle b\rangle,$$

$$x = A^{-1}b.$$

3.4. Boundary conditions, equilibrium distribution and gyro-average operator

The perturbed distribution function is periodic in both θ and ζ directions which satisfies

$$\delta f\left(\psi,\theta+2\pi,\zeta,V_{\parallel},\mu\right)=\delta f\left(\psi,\theta,\zeta,V_{\parallel},\mu\right),$$
$$\delta f\left(\psi,\theta,\zeta+2\pi,V_{\parallel},\mu\right)=\delta f\left(\psi,\theta,\zeta,V_{\parallel},\mu\right).$$

For other two directions ψ and $V_{\parallel}$ the fixed boundary condition is assumed, i.e.,

$$\delta f\left(\psi,\theta,\zeta,V_{\parallel},\mu\right)=\delta f\left(\psi_b,\theta,\zeta,V_{\parallel},\mu\right),\ \ if\ \psi>\psi_b,$$
$$\delta f\left(\psi,\theta,\zeta,V_{\parallel},\mu\right)=\delta f\left(\psi_a,\theta,\zeta,V_{\parallel},\mu\right),\ \ if\ \psi<\psi_a,$$

with $[\psi_a,\psi_b]$ the computation domain in radial direction. In numerical computation, if a particle moves out of the computational boundary of ψ and $V_{\parallel}$, it will be forced to stay on the boundary so that the interpolation points are always inside the computational domain.

For the QN equation, the fixed boundary condition is applied, i.e.,

$$\delta\phi\left(\psi_a,\theta,\zeta\right)=\delta\phi\left(\psi_b,\theta,\zeta\right)=0.$$

The equilibrium distribution F_{eq} should be a constant of motion so that Eq. (23) is valid. In our simulation, the equilibrium distribution can be chosen as a local Maxwellian due to the application of the δf method. The ion equilibrium distribution is written as

$$F_{eq}\left(\psi,\theta,\zeta,V_{\parallel},\mu\right)=\left(\frac{m_i}{2\pi T_i}\right)^{\frac{3}{2}}n_{0i}exp\left(-\frac{\frac{1}{2}m_iV_{\parallel}^2+\mu B}{T_i}\right),$$

where $n_{0i}\left(\psi\right)$ and $T_i\left(\psi\right)$ are particle density and temperature, respectively. The partial derivatives of F_{eq}, which appear in Eq. (25) can be given as follows

$$\partial_{\psi}F_{eq}=\left(\frac{n_i'}{n_i}+\left(\frac{\frac{1}{2}m_iV_{\parallel}^2+\mu B}{T_i}-\frac{3}{2}\right)\frac{T_i'}{T_i}-\frac{\mu\partial_{\psi}B}{T_i}\right)F_{eq},$$
$$\partial_{\theta}F_{eq}=-\frac{\mu\partial_{\theta}B}{T_i}F_{eq},$$
$$\partial_{\zeta}F_{eq}=0,$$
$$\partial_{V_{\parallel}}F_{eq}=-\frac{m_iV_{\parallel}}{T_i}F_{eq}.$$

The gyro-average operator is approximated by a four-point discrete sum method [26] which is valid for $k\rho<2$.

3.5. Parallelization strategy

The NLT code is parallelized by hybrid MPI + OpenMP programming. The distribution function is decomposed by magnetic moment μ and distributed to different processes. For the QN equation, the inverse matrix A^{-1} is stored distributedly on different processes. The loops within a process are parallelized with OpenMP.

4. Simulation results

4.1. Rosenbluth–Hinton test

In this subsection, the Rosenbluth–Hinton (R–H) test is performed. It has been predicted that [27] an $E\times B$ flow imposed in toroidal plasmas as an initial pulse will excite a geodesic acoustic mode (GAM) [28] oscillation. This poloidal flow will relax to a stationary value which is called residual flow due to Landau damping. The analytical theory of GAM frequency and damping rate can be found in Ref. [29] and the residual flow level is calculated in Ref. [27].

A concentric circles equilibrium is used for simulation with parameters $B_0=1.5$ T, $R_0=1.25$ m, $a=0.45$ m, where a and R_0 are the minor radius and major radius, respectively. The temperature and density profile are both set to be constants as $T_i=0.15$ kev, $n_{i0}=10^{19}/\mathrm{m}^3$. The radial domain taken in the simulation is $[r_a,r_b]=[0.45a,0.6a]$ so that $k_r\rho_i=0.11$, where $k_r=2\pi/\left(r_b-r_a\right)$ is wave number in radial direction. To excite the $E\times B$ flow, a sinusoidal perturbation of the flux surface averaged ion density, $\delta n\times sin\left(k_r\left(r-r_a\right)\right)$, is imposed in the radial direction. Here, the perturbation amplitude δn is chosen as $\delta n/n_{i0}=10^{-5}$. Since GAM is a electrostatic mode with toroidal symmetry, only one grid in toroidal direction is needed, that is $n_{\zeta}=1$. The grid resolution $\left(n_{\psi}\times n_{\theta}\times n_{V_{\parallel}}\times n_{\mu}\right)$ for $\left(\psi,\theta,V_{\parallel},\mu\right)$ are set as $(80\times64\times128\times64)$. The computational domain in phase space used for R–H test is $V_{\parallel}\in[-5V_{ti},5V_{ti}]\times\mu\in[0,13T_i/B_0]$. The time step in computation is set as $\Delta t=0.019R_0/V_{ti}$. In Fig. 1, the evolution of E_r from both numerical simulation and analytical theory, with $\tau=T_e/T_i=0$, are plotted and compared. It can be seen that the numerical results of GAM frequency, damping rate and residual flow level are all well consistent with theoretical predictions.

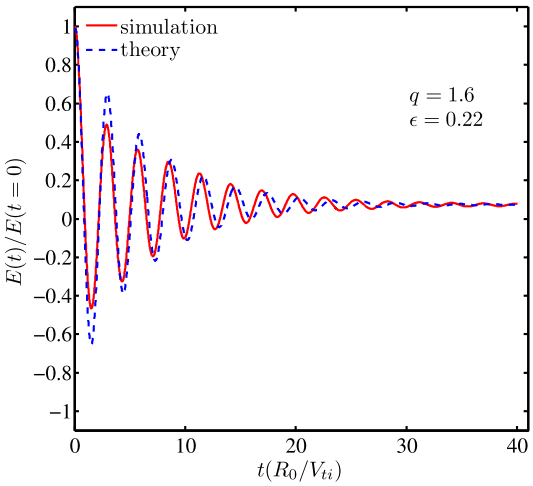

Fig. 1. GAM radial electric filed evolution with $q = 1.6$, $\epsilon = 0.22$. The theoretical prediction for GAM frequency, damping rate and residual flow level are given in Ref. [29] and Ref. [27].

4.2. ITG Cyclone test

In this subsection, a set of linear ion temperature gradient simulations are performed for the Cyclone-test [30] like parameters. To verify the simulation results, a comparison between numerical results of the NLT code and the GENE code is presented. The parameters used in our simulation are set as close as possible to those in Ref. [11]. Once again, a concentric circles equilibrium is used with parameters $R_0 = 1.6714$ m, $a = 0.6043$ m, $B_0 = 1.9$ T. The safety factor profile is set as

$$q = \frac{0.864 + 2.27\left(\frac{r}{a}\right)^2}{\sqrt{1 - \left(\frac{r}{R_0}\right)^2}},$$

so that $q(r_0) = 1.455$ and $\hat{s}(r_0) = 0.826$, with $r_0 = 0.5a$ and $\hat{s} = (r/q)\,dq/dr$ the magnetic shear. The temperature and density profile are set as

$$T(r) = T_0 exp\left[-\kappa_T \frac{a}{R_0}\Delta_T tanh\left(\frac{(r - r_0)/a}{\Delta_T}\right)\right],$$
$$N(r) = N_0 exp\left[-\kappa_N \frac{a}{R_0}\Delta_N tanh\left(\frac{(r - r_0)/a}{\Delta_N}\right)\right],$$

with $T_0 = 1.9693$ kev, $N_0 = 10^{19}/\mathrm{m}^3$, $\kappa_T = 6.9589$, $\kappa_N = 2.232$, $\Delta_T = \Delta_N = 0.3$. Here, $\tau = T_e/T_i = 1$ is assumed. These profiles are plotted in Fig. 2.

For the linear ITG simulation, a toroidal mode number is given, which is denoted by n_0, so that only this mode in toroidal direction is kept. Therefore, the simulation domain for ζ can be reduced to $[0, 2\pi/n_0)$ and the periodic boundary condition in toroidal direction is applied for all variables. A toroidal mode filtering is utilized so that only the fundamental mode in $\zeta \in [0, 2\pi/n_0)$ is kept. The size of radial simulation box is $160\rho_i$. The computational domain in phase space for the Cyclone test is $V_\parallel \in [-3V_{ti}, 3V_{ti}] \times \mu \in [0, 9T_i/B_0]$. A dimensionless number $k_\theta\rho_i$ is used to represent the mode number, where k_θ is defined by $k_\theta = n_0 q_0/r_0$. The grid resolution $\left(n_\psi \times n_\theta \times n_\zeta \times n_{V_\parallel} \times n_\mu\right)$ are set as $(160 \times 128 \times 32 \times 64 \times 32)$ and $(160 \times 512 \times 32 \times 64 \times 32)$ for $k_\theta\rho_i < 0.3$ and $k_\theta\rho_i \geq 0.3$, respectively. In Fig. 3, the mode frequency and growth rate for different mode numbers are shown; it can be seen that the simulation results from two codes are consistent with each other. In Fig. 4, the mode amplitude and mode structure for $k_\theta\rho_i = 0.3$ are shown.

To end this section, we note that in the above NLT simulations, the usual damping buffer region near the radial boundary of computational domain used in many other codes is not needed here. In comparing the GAM simulation with our previous work [13], we conclude that the computation efficiency of the NLT code is comparable to the previous semi-Lagrangian operator splitting method.

5. Summary

In this work, we have developed a new continuum code to solve the nonlinear gyrokinetic equation for the parallel simulation of electrostatic modes in a tokamak fusion plasma. The numerical scheme is based on the recently developed I-transform theory which decouples the perturbed motion from the unperturbed motion. Therefore, the unperturbed motion

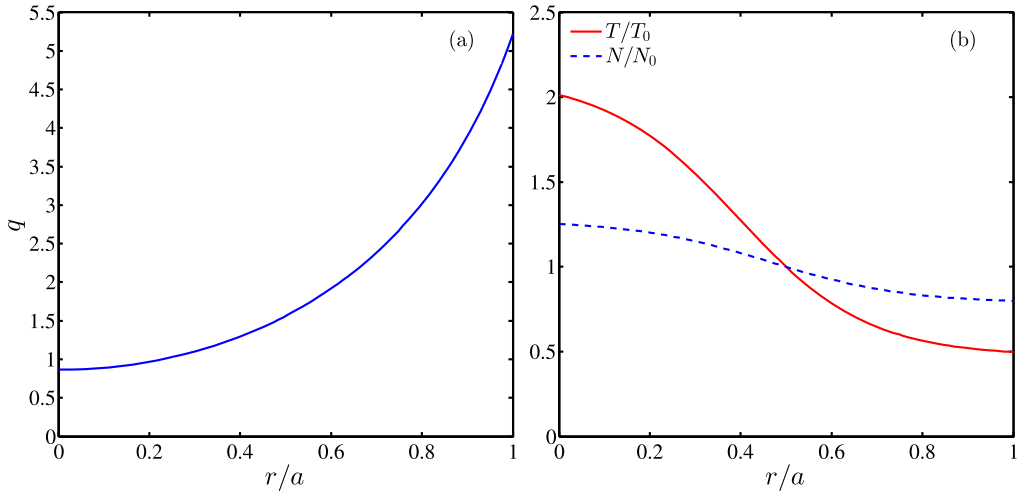

Fig. 2. (a) q profile, (b) temperature and density profile.

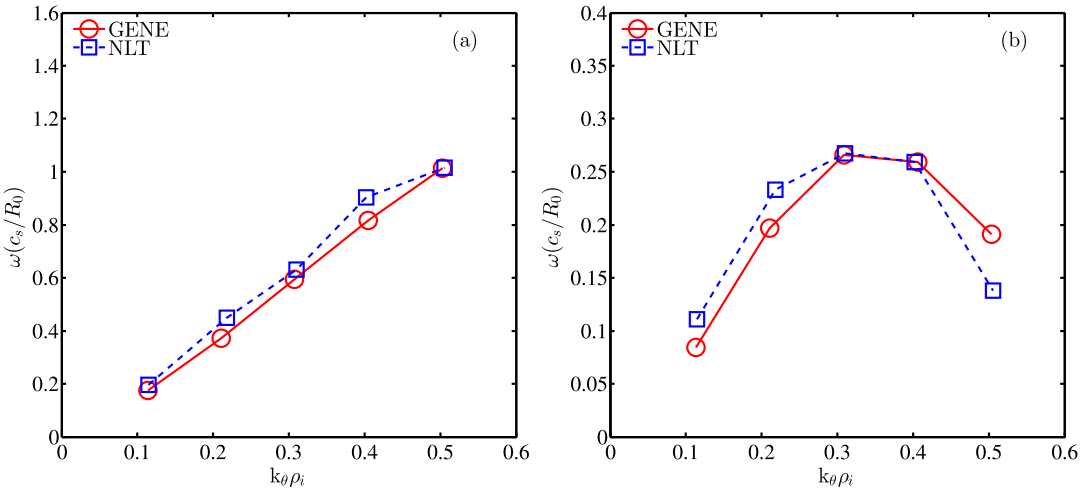

Fig. 3. Comparison of linear ITG frequency (a) and growth rate (b) between GENE and NLT with adiabatic electron and $\tau = 1$.

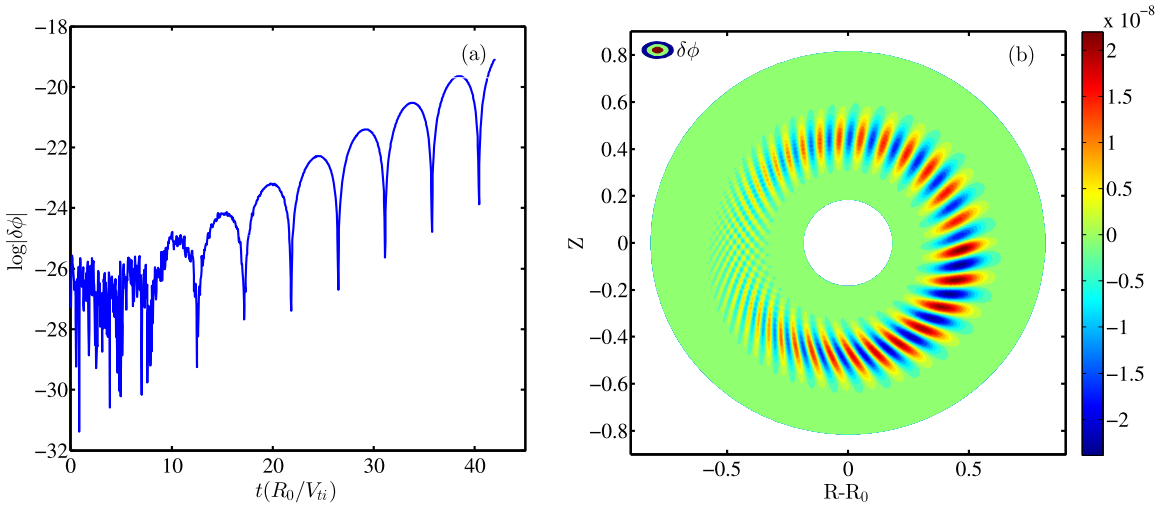

Fig. 4. Perturbation potential evolution (a) and ITG mode structure (b) for $n_0 = 33$.

can be computed before evolving the distribution function. The effects of the unperturbed motion on the evolution of distribution function are evaluated by using the semi-Lagrangian method and a 4D B-spline interpolation method, while the effects of the perturbed motion on the evolution are evaluated by the I-transform method which needs only to integrate the perturbed potential along the unperturbed orbit.

We have verified the NLT code by running the Rosenbluth–Hinton test and the Cyclone base test of linear ITG mode. The NLT simulation results of the GAM agree well with the analytical theory. The linear ITG mode simulation results of the NLT code agree well with the results by the GENE code, an Eulerian continuum code. The preliminary results show that the efficiency of the I-transform method used in the NLT code to solve the nonlinear gyrokinetic equation is comparable with the previous operator-splitting semi-Lagrangian method. For the test of the NLT code, such as the nonlinear simulation of ITG mode, will be reported in the near future.

Acknowledgements

One of the authors (Lei Ye) would like to thank Dr. Yang Chen at the University of Colorado, Boulder for useful discussions on the cyclone test case. This work was supported by the National Natural Science Foundation of China under Grant No. 11175178, No. 11375196, No. 11505240, No. 11405174 and the National ITER program of China under Contract No. 2014GB113000.

Appendix A. Coefficients in QN equation

Let $\beta = \frac{e_i^2 \rho_{ti}^2}{T_i}$, the coefficients in Eq. (34) are given as follows.

$$c_1 = \beta n_{0i} g^{\psi\psi},$$
$$c_2 = \beta n_{0i} (g^{\theta\theta} - \frac{1}{\mathcal{J}^2 B^2}),$$
$$c_3 = \beta n_{0i} 2 g^{\psi\theta},$$
$$c_4 = \beta \frac{1}{\mathcal{J}} [\partial_\psi (\mathcal{J} g^{\psi\psi} n_{0i}) + \partial_\theta (\mathcal{J} g^{\theta\psi} n_{0i})],$$
$$c_5 = \beta \frac{1}{\mathcal{J}} [\partial_\psi (\mathcal{J} g^{\psi\theta} n_{0i}) + \partial_\theta (\mathcal{J} g^{\theta\theta} n_{0i}) - \partial_\theta (\frac{n_{0i}}{\mathcal{J} B^2})],$$
$$c_6 = -\frac{e n_{0e}}{T_e}.$$

By taking the magnetic-flux-surface average of Eq. (34), one gets the averaged QN equation,

$$\langle L \rangle \langle \delta\phi \rangle = -e_i \langle \delta n_i^g \rangle,$$

with $\langle L \rangle = \left\langle \beta n_{0i} g^{\psi\psi} \right\rangle \partial_{\psi^2}^2 + \left\langle \beta \frac{1}{\mathcal{J}} [\partial_\psi (\mathcal{J} g^{\psi\psi} n_{0i}) \right\rangle \partial_\psi$. Here, the approximation $\langle \mathcal{L} \delta\phi \rangle = \langle \mathcal{L} \rangle \langle \delta\phi \rangle$ is applied. Thus the coefficients in Eq. (35) are given by

$$d_1 = \left\langle \beta n_{0i} g^{\psi\psi} \right\rangle,$$
$$d_2 = \left\langle \beta \frac{1}{\mathcal{J}} [\partial_\psi (\mathcal{J} g^{\psi\psi} n_{0i}) \right\rangle.$$

Appendix B. High dimensional B-spline interpolation

In the NLT code, high dimensional (3D and 4D) spline interpolation is performed by using the tensor product of B-spline [31].

Suppose that a one-dimensional function $f = f(x)$ is approximated by B-splines $P_f = \alpha_i \mathcal{B}_i(x)$ which satisfy the condition $f(x_i) = P_f(x_i)$ at each grid node x_i. And in another dimension $g(y)$ is approximated by P_g, then interpolations in two dimensions can be done:

$$w(x, y) = \alpha_{ij} \mathcal{B}_i(x) \mathcal{B}_j(y).$$

For each grid node (x_r, y_s), the coefficients satisfy the condition

$$w(x_r, y_s) = \alpha_{ij} \mathcal{B}_i(x_r) \mathcal{B}_j(y_s).$$

The 3D and 4D B-spline tensor product interpolation can be done in the similar way:

$$w(x, y, z) = \alpha_{ijk} \mathcal{B}_i(x) \mathcal{B}_j(y) \mathcal{B}_k(z),$$
$$w(x, y, u, v) = \alpha_{ijkl} \mathcal{B}_i(x) \mathcal{B}_j(y) \mathcal{B}_k(u) \mathcal{B}_l(v).$$

Usually, only the data at the grid nodes are not enough to determine the coefficients completely. Different boundary conditions may be applied. For example, when the cubic B-spline (its order is 4) is used in one dimension, the first order derivative at both ends of the interval may be added to determine the coefficients completely [32]. Without providing these two first order derivative, not-a-knot condition can also help to determine the coefficients. If the knot sequence is constructed periodically, and so do the coefficients, then a rigorous periodic condition can be obtained. Here rigorous periodic condition means the value and possible derivatives of function exactly equal at the first and the last grid node.

In the NLT code, the rigorous periodic condition is applied in poloidal and toroidal dimensions, not-a-knot condition is applied in other dimensions. In order to reduce the computation cost, the parabolic B-spline (its order is 3) is used.

Appendix C. Discretization of QN equation

For a periodic function $f(\theta)$, let

$$f = (f_1, f_2, \cdots, f_n)^{\mathrm{T}},$$

with

$$f_j = f(\theta_j), \quad \theta_j = \frac{2\pi(j-1)}{n}, \quad j = 1, 2, \cdots, n.$$

The first order and second order derivatives of f can be evaluated by the first order and the second order Fourier derivative matrices, respectively, as [33]

$$f' = D_1 f, \tag{C.1}$$

$$f'' = D_2 f. \tag{C.2}$$

Here, D_1 and D_2 are $m \times m$ matrices defined by

$$(D_1)_{ij} = \begin{cases} \frac{1}{2}(-1)^{(i+j)} cot[\frac{(i-j)\pi}{n}], & i \neq j \\ 0, & i = j \end{cases} \tag{C.3}$$

$$(D_2)_{ij} = \begin{cases} \frac{1}{4}(-1)^{(i+j)} n + \frac{(-1)^{i+j+1}}{2sin^2[\frac{(i-j)\pi}{n}]}, & i \neq j \\ -\frac{(n-1)(n-2)}{12}. & i = j \end{cases} \tag{C.4}$$

For a non-periodic function $g(\psi)$ $\psi \in (\psi_a, \psi_b)$, let

$$g = (g_1, g_2, \cdots, g_n)^{\mathrm{T}},$$

with

$$g_i = g(\psi_i), \quad \psi_i = \psi_i + \frac{(\psi_b - \psi_a)(i-1)}{m-1}, \quad i = 1, 2, \cdots, m.$$

Similarly, the finite difference derivative matrix for the radial derivative can be derived from Eq. (38) and Eq. (39) as

$$F_1 = \frac{1}{12\Delta\psi} \begin{bmatrix} -25 & 48 & -36 & 16 & -3 & & & & & \\ -3 & -10 & 18 & -6 & 1 & & & & & \\ 1 & -8 & 0 & 8 & -1 & & & & & \\ & 1 & -8 & 0 & 8 & -1 & & & & \\ & & & \cdots & \cdots & \cdots & & & & \\ & & & 1 & -8 & 0 & 8 & -1 & & \\ & & & & 1 & -8 & 0 & 8 & -1 & \\ & & & & -1 & 6 & -18 & 10 & 3 & \\ & & & & 3 & -16 & 36 & -48 & 25 & \end{bmatrix}_{m\times m}, \tag{C.5}$$

$$F_2 = \frac{1}{12\Delta\psi^2} \begin{bmatrix} 35 & -104 & 114 & -56 & 11 & & & & & \\ 11 & -20 & 6 & 4 & -1 & & & & & \\ -1 & 16 & -30 & 16 & -1 & & & & & \\ & -1 & 16 & -30 & 16 & -1 & & & & \\ & & & \cdots & \cdots & \cdots & & & & \\ & & & -1 & 16 & -30 & 16 & -1 & & \\ & & & & -1 & 16 & -30 & 16 & -1 & \\ & & & & -1 & 4 & 6 & -20 & 11 & \\ & & & & 11 & -56 & 114 & -104 & 35 & \end{bmatrix}_{m\times m}. \tag{C.6}$$

Now we turn to a 2D function and its derivatives. For a 2D $m \times n$ matrix Φ defined by

$$\Phi_{i,j} = \delta\phi\left(\psi_i, \theta_j\right), \quad i = 1, 2, \cdots, m, \quad j = 1, 2, \cdots, n, \tag{C.7}$$

we map it onto a $m \times n$ vector x defined by

$$x_k = \Phi_{i(k),j(k)}, \quad k = 1, 2, \cdots, m \times n = N \tag{C.8}$$

with x explicitly written as

$$x = \left(\Phi_{1,1}, \quad \Phi_{1,2}, \quad \cdots, \quad \Phi_{1,n}; \quad \Phi_{2,1}, \quad \Phi_{2,2}, \quad \cdots \quad \Phi_{2,n}; \quad \cdots, \quad \Phi_{m,1}, \quad \Phi_{m,2}, \quad \cdots \quad \Phi_{m,n}\right)^{\mathrm{T}}. \tag{C.9}$$

Here, the map $k \leftrightarrow (i(k), j(k))$ can be expressed as

$$i(k) = (k-1)/n + 1, \tag{C.10}$$

$$j(k) = mod(k, n), \tag{C.11}$$

$$k = n \times (i-1) + j. \tag{C.12}$$

Then the 2D derivative matrix can be constructed from the 1D derivative matrix given above. For example, let's denote the 1st order partial derivative matrix for ∂_θ by $(D_\theta)_{N\times N}$, which satisfies

$$D_\theta x = x_\theta, \tag{C.13}$$

where $x_\theta = \left((\Phi_\theta)_{1,1}, (\Phi_\theta)_{1,2}, \cdots, (\Phi_\theta)_{1,n}; (\Phi_\theta)_{2,1}, (\Phi_\theta)_{2,2}, \cdots (\Phi_\theta)_{2,n}; \cdots; (\Phi_\theta)_{m,1}, (\Phi_\theta)_{m,2}, \cdots (\Phi_\theta)_{m,n}\right)^{\mathrm{T}}$, with $(\Phi_\theta)_{i,j} = \frac{\partial}{\partial\theta}\delta\phi\left(\psi_i, \theta_j\right)$. The k_0th row of D_θ can be constructed as follows.

Step 1. Set $D_\theta(k_0, k) = 0$ for $k = 1, 2, \cdots N$.

Step 2. Compute $i(k_0)$ and $j(k_0)$ by Eq. (C.10) and Eq. (C.11). From Eq. (C.1), one has

$$\sum_{l=1}^{n} (D_1)_{j(k_0),l}\, \Phi_{i(k_0),l} = (\Phi_\theta)_{i(k_0),j(k_0)} = (x_\theta)_{k_0}.$$

Step 3. Compute $k' = k(i(k_0), l)$, $(l = 1, 2, \cdots n)$ by Eq. (C.12) and set $D_\theta\left(k_0, k'\right) = (D_1)_{j(k_0),l}$.

For the partial derivative with variable coefficient such as $c_5\partial_\theta$ in Eq. (34), the derivative matrix C_5 can be calculated from D'_θ by

$$C_5\left(k_0, k'\right) = c\left(i(k_0), j(k_0)\right) D_\theta\left(k_0, k'\right), \quad k' = 1, 2, \cdots, N. \tag{C.14}$$

Similarly, all the derivative matrix $\{C_i\}_{i=1}^{6}$ on the LHS of Eq. (34) can be calculated and the total derivative matrix can be denoted by

$$A = \sum_{i=1}^{6} C_i. \tag{C.15}$$

Let's denote the RHS of Eq. (34) by $s(\psi, \theta)$. By discretizing s to an $m \times n$ vector b according to Eq. (C.9), one gets the linear algebraic equations for Eq. (34) as

$$Ax = b. \tag{C.16}$$

References

[1] F. Hinton, R. Hazeltine, Theory of plasma transport in toroidal confinement systems, Rev. Mod. Phys. 48 (2) (1976) 239.
[2] W. Horton, Drift waves and transport, Rev. Mod. Phys. 71 (3) (1999) 735.
[3] D. Batchelor, M. Beck, A. Becoulet, R. Budny, C. Chang, P. Diamond, J. Dong, G. Fu, A. Fukuyama, T. Hahm, et al., Simulation of fusion plasmas: current status and future direction, Plasma Sci. Technol. 9 (3) (2007) 312.
[4] A. Brizard, T. Hahm, Foundations of nonlinear gyrokinetic theory, Rev. Mod. Phys. 79 (2) (2007) 421.
[5] X. Garbet, Y. Idomura, L. Villard, T. Watanabe, Gyrokinetic simulations of turbulent transport, Nucl. Fusion 50 (4) (2010) 043002.
[6] Z. Lin, W. Tang, W. Lee, Gyrokinetic particle simulation of neoclassical transport, Phys. Plasmas (1994–present) 2 (8) (1995) 2975–2988.
[7] Y. Chen, S.E. Parker, A δf particle method for gyrokinetic simulations with kinetic electrons and electromagnetic perturbations, J. Comput. Phys. 189 (2) (2003) 463–475.
[8] M. Fivaz, S. Brunner, G. De Ridder, O. Sauter, T. Tran, J. Vaclavik, L. Villard, K. Appert, Finite element approach to global gyrokinetic particle-in-cell simulations using magnetic coordinates, Comput. Phys. Commun. 111 (1) (1998) 27–47.
[9] W. Dorland, F. Jenko, M. Kotschenreuther, B. Rogers, Electron temperature gradient turbulence, Phys. Rev. Lett. 85 (26) (2000) 5579.
[10] J. Candy, R. Waltz, An Eulerian gyrokinetic-Maxwell solver, J. Comput. Phys. 186 (2) (2003) 545–581.
[11] T. Görler, X. Lapillonne, S. Brunner, T. Dannert, F. Jenko, F. Merz, D. Told, The global version of the gyrokinetic turbulence code gene, J. Comput. Phys. 230 (18) (2011) 7053–7071.

[12] V. Grandgirard, Y. Sarazin, P. Angelino, A. Bottino, N. Crouseilles, G. Darmet, G. Dif-Pradalier, X. Garbet, P. Ghendrih, S. Jolliet, et al., Global full-f gyrokinetic simulations of plasma turbulence, Plasma Phys. Control. Fusion 49 (12B) (2007) B173.
[13] L. Ye, W. Guo, X. Xiao, S. Wang, Numerical simulation of geodesic acoustic modes in a multi-ion system, Phys. Plasmas (1994–present) 20 (7) (2013) 072501.
[14] J.-M. Kwon, D. Yi, X. Piao, P. Kim, Development of semi-Lagrangian gyrokinetic code for full-f turbulence simulation in general tokamak geometry, J. Comput. Phys. 283 (2015) 518–540.
[15] G. Strang, On the construction and comparison of difference schemes, SIAM J. Numer. Anal. 5 (3) (1968) 506–517.
[16] V. Grandgirard, M. Brunetti, P. Bertrand, N. Besse, X. Garbet, P. Ghendrih, G. Manfredi, Y. Sarazin, O. Sauter, E. Sonnendrücker, et al., A drift-kinetic semi-Lagrangian 4d code for ion turbulence simulation, J. Comput. Phys. 217 (2) (2006) 395–423.
[17] S. Wang, Transport formulation of the gyrokinetic turbulence, Phys. Plasmas (1994–present) 19 (6) (2012) 062504.
[18] S. Wang, Kinetic theory of weak turbulence in plasmas, Phys. Rev. E 87 (6) (2013) 063103.
[19] S. Wang, Lie-transform theory of transport in plasma turbulence, Phys. Plasmas (1994–present) 21 (7) (2014) 072312.
[20] Y. Xu, Z. Dai, S. Wang, Nonlinear gyrokinetic theory based on a new method and computation of the guiding-center orbit in tokamaks, Phys. Plasmas (1994–present) 21 (4) (2014) 042505.
[21] Z. Dai, Y. Xu, L. Ye, X. Xiao, S. Wang, A new continuum approach for nonlinear kinetic simulation and transport analysis, Phys. Plasmas (1994–present) 22 (2) (2015) 022301.
[22] Y. Xu, X. Xiao, S. Wang, Linear gyrokinetic theory and computation of the gyrocenter motion based on the exact canonical variables for axisymmetric tokamaks, Phys. Plasmas (1994–present) 18 (4) (2011) 042505.
[23] R.B. White, The Theory of Toroidally Confined Plasmas, World Scientific, 2001.
[24] Y. Idomura, M. Ida, T. Kano, N. Aiba, S. Tokuda, Conservative global gyrokinetic toroidal full-f five-dimensional Vlasov simulation, Comput. Phys. Commun. 179 (6) (2008) 391–403.
[25] X. Xiao, S. Wang, Explicit Runge–Kutta integrator with Hamiltonian correction for long-time simulations of guiding-center orbit in tokamak configurations, Phys. Plasmas (1994–present) 15 (12) (2008) 122511.
[26] W. Lee, Gyrokinetic particle simulation model, J. Comput. Phys. 72 (1) (1987) 243–269.
[27] M. Rosenbluth, F. Hinton, Poloidal flow driven by ion-temperature-gradient turbulence in tokamaks, Phys. Rev. Lett. 80 (4) (1998) 724.
[28] N. Winsor, J.L. Johnson, J.M. Dawson, Geodesic acoustic waves in hydromagnetic systems, Phys. Fluids (1958–1988) 11 (11) (1968) 2448–2450.
[29] H. Sugama, T.-H. Watanabe, Collisionless damping of geodesic acoustic modes, J. Plasma Phys. 72 (06) (2006) 825–828.
[30] A. Dimits, G. Bateman, M. Beer, B. Cohen, W. Dorland, G. Hammett, C. Kim, J. Kinsey, M. Kotschenreuther, A. Kritz, et al., Comparisons and physics basis of tokamak transport models and turbulence simulations, Phys. Plasmas (1994–present) 7 (3) (2000) 969–983.
[31] C. de Boor, A Practical Guide to Splines, vol. 27, Springer, 2001.
[32] G. Latu, V. Grandgirard, J. Abiteboul, N. Crouseilles, G. Dif-Pradalier, X. Garbet, P. Ghendrih, M. Mehrenberger, Y. Sarazin, E. Sonnendrücker, Improving conservation properties of a 5d gyrokinetic semi-Lagrangian code, Eur. Phys. J. D 68 (11) (2014) 1–16.
[33] C. Canuto, M.Y. Hussaini, A. Quarteroni, T.A. Zang, Spectral Methods in Fluid Dynamics, Tech. rep. Springer, 1988.